J. Appl. Comput. Mech., xx(x) (2026) 1-16
DOI: 10.22055/jacm.2026.49656.6137

ISSN: 2383-4536
jacm.scu.ac.ir

Shahid Chamran University of Ahvaz

Journal of Applied and Computational Mechanics

Research Paper

Comparative Analysis of Artificial Neural Networks and Response Surface Methods for Mixed Convective Heat Transfer in a Rectangular Channel with Heated Diamond-Shaped Obstacles

Md. Noor-A-Alam Siddiki, Md. Shahinur Islam, Farjana Habiba

Department of Computer Science and Engineering, Stamford University, Bangladesh,
Email: siddiki@stamforduniversity.edu.bd (Md.N.A.S.); shahinislam@stamforduniversity.edu.bd (Md.S.I.); farjanahabiba@stamforduniversity.edu.bd (F.H.)

Received August 02 2026; Revised September 30 2026; Accepted for publication September 30 2026.
✉ Corresponding author: Md. Noor-A-Alam Siddiki (siddiki@stamforduniversity.edu.bd)
© 2026 Published by Shahid Chamran University of Ahvaz

Abstract. The mixed convective heat transfers and flow characteristics of a non-Newtonian power-law hybrid nanofluid, Al_2O_3 - CNT/water) in an open rectangular channel containing two heated diamond-shaped blocks with a bottom inlet, two top outlets, and isothermal cold side walls, are investigated numerically. The non-dimensional controlling transport equations are computed numerically using COMSOL Multiphysics, while the left vertical wall is kept at an identical cold temperature (T_c). The analysis considers a wide range of controlling parameters: nanoparticle volume fraction (ϕ = 0.00, 0.01, 0.02, 0.04), Richardson number (Ri = 1.0, 2.0, 4.0, 6.0), Reynolds number (Re = 50, 100, 200, 400), Power law index (n = 0.6, 0.8, 1.0, 1.2), and inlet/outlet width (W_{in} = W_{out} = 0.1). The results exhibit that the governing parameters have a substantial effect on the thermal performance of the rectangular channel: higher values of the power-law index (n) reduced heat transfer, while higher values of the nanoparticle volume fraction (ϕ), Richardson number (Ri), and Reynolds number (Re) increase it. While comparative analyses using Response Surface Methodology (RSM) and Artificial Neural Networks (ANNs) confirm their efficacy in accurately predicting the average Nusselt number, Nu_{av} detailed flow and thermal characteristics are presented, providing effective tools for designing and optimizing of hybrid nanofluid-based thermal systems.

Keywords: Nanofluids, Streamline, Isotherm, Power law index, Comsol Multiphysics.

1. Introduction

Computational investigations of intricate nanofluid flow and heat transfer problems have increasingly included artificial intelligence and machine learning approaches in recent years. Alarabi et al. [1] investigated the magnetorheological dynamics of a dusty nanofluid using artificial neural networks and hybrid fourth-order numerical techniques, showcasing the potential of AI-based methods for difficult flow characteristic prediction. In order to anticipate heat and mass transfer in a wavy annular cavity filled with a nanofluid and heterogeneous media, Aly et al. [2] further developed a mesh-free and artificial intelligence-based framework. Additionally, Alsedais et al. [3] used entropic analysis and an artificial neural network to evaluate and optimize MHD natural bio-convection in a square nanofluid-filled enclosure. Similarly, Elsedais et al. [4] demonstrated the efficacy of ANN-based models in forecasting and evaluating intricate thermal-flow properties by proposing an AI-driven FVM–ANN model for entropy analysis of MHD natural bio convection in nanofluid-filled porous cavities. Taking into account the impacts of thermal radiation and heat generation/absorption, Sharma and Mishra [5] examined the flow and heat transfer properties of metal and metallic oxide nanofluids at a shrinking surface. Using a central composite design, Srivastava and Sharma [6] investigated magnetically dissipative Darcy-Forchheimer hybrid nanofluid flow over an expanding sheet, emphasizing the impact of important governing parameters on the flow and heat transfer characteristics. In a different work, Srivastava and Sharma [7] optimized the thermal transfer rate of hybrid nanofluid flow over a porous stretched sheet with varied slip conditions using response surface methodology.

Additionally, Sharma et al. [8] critically analyzed non-Newtonian Sisko fluids, highlighting their flow properties and possible uses in a range of industrial engineering domains. Since the pioneering work of Choi and Eastman [9], nanofluids have been explored extensively for their potential to improve heat exchange efficiency in electronic cooling, solar energy systems, biomedical devices, and nuclear reactors [10-12]. Including nanoparticles, such as Al_2O_3, CuO, SiO_2, and TiO_2, in base fluids leads to enhanced thermal conductivity, modified viscosity, and altered flow behavior [13-15]. In addition, stability and concentration of nanoparticles (i.e., volume fraction ϕ) are recognized as critical factors influencing nanofluid performance [15, 16]. In recent years, the concept of hybrid nanofluids has emerged, where more than different kinds of nanoparticle are dispersed within the base fluid [17, 18]. Hybrid nanofluids combine the advantages of each constituent nanoparticle, resulting in synergistic effects that further enhance thermal properties compared with single-component nanofluids [19, 20]. For example, it has been

Published online: October 31 2026

demonstrated that combining metallic and carbon-derived nanoparticles, like Al_2O_3 and carbon nanotubes (CNTs), can greatly enhance thermal conductivity while preserving desired rheological behavior [21-23]. Hybrid nanofluids have therefore been increasingly investigated for applications in compact heat exchangers, automotive cooling, and renewable energy systems [24-26]. Apart from Newtonian fluids, many practical fluids encountered in industry exhibit non-Newtonian behavior, such as power-law fluids [27, 28]. Examples include polymeric solutions, slurries, food processing liquids, and biomedical fluids [29, 10]. Shear rate has a significant impact on the density of non-Newtonian fluids, which introduces additional complexity in their convective transport behavior [30, 31]. Consequently, understanding mixed convection of non-Newtonian nanofluids is vital for optimizing numerous engineering processes [32, 33]. The study of mixed convection where both natural and forced convection mechanisms contribute within enclosures has been of particular interest due to its relevance in solar collectors, building ventilation, heat exchangers, and nuclear waste storage [34-36]. Enclosure geometry, boundary conditions, and the presence of obstacles or fins strongly influence heat and mass transfer in such systems [37, 38]. Numerical simulations and computational tools, such as COMSOL Multiphysics and finite element methods, have been widely employed to investigate these phenomena [39, 40]. Fins are commonly integrated into enclosures to increase surface area, improve heat transfer, and induce favorable flow structures [41-43]. The placement, size, and orientation of fins significantly affect the overall thermal performance of enclosures [44, 45]. In particular, attaching heated fins to vertical or horizontal walls can alter circulation patterns, improving convective transport [46]. Building on these considerations, modeling mixed convection of a non-Newtonian hybrid nanofluid (Al_2O_3, CNT/H_2O) inside an open rectangular enclosure with two heated fins affixed to the right wall is the main focus of this investigation. With an entrance at the bottom and a vent at the top, the enclosure's design is practical for open-cavity cooling systems.

Governing non-dimensional transport equations are solved computationally using COMSOL Multiphysics, with a comprehensive parametric analysis performed across nanoparticle volume fraction, Richardson number, Reynolds number, power-law index, and inlet/outlet opening size. This investigation's combined consideration of hybrid nanofluid characteristics is what makes it unique., non-Newtonian shear-dependent rheology, and fin-enhanced enclosure design under mixed convection conditions. Although several studies have addressed mixed convection in enclosures using Newtonian nanofluids [13, 20, 38], limited research has explored the interplay of hybrid nanofluids and power-law behavior in open cavities with structural modifications such as fins. This investigation contributes to bridging this gap, offering insights into flow dynamics, thermal fields, and overall heat transfer performance that may guide the design of advanced thermal management systems. Inspired by the aforementioned research gaps, the current study examines mixed convective heat transfer of a non-Newtonian hybrid nanofluid that flows through a rectangular channel with heated diamond-shaped obstacles and contains alumina-carbon nanotube (Al_2O_3, CNT) nanoparticles scattered in water (H_2O). The COMSOL Multiphysics simulation platform is used to solve the governing equations numerically. The streamline and temperature distributions, average Nusselt number, temperature profiles, velocity profiles, and the Reynolds number (Re), Richardson number (Ri), nanoparticle volume fraction (ϕ), and flow behavior index (n) are all systematically investigated. Additionally, prediction models for the average Nusselt number are developed using Response Surface Methodology (RSM) and Artificial Neural Networks (ANN), and their predictive performances are compared. According to the numerical results, raising Re, Ri, and ϕ strengthens convective transport and improves the hybrid nanofluid's effective thermal conductivity, which raises the average Nusselt number. In contrast, in the examined circumstances, the average Nusselt number falls as the power-law index (n) rises. Additionally, using hybrid nanoparticles increases heat transfer within the rectangular channel by intensifying flow circulation and vortex formations surrounding the heated barriers. The results of this study show the usefulness of RSM and ANN as trustworthy predictive tools for the design and optimization of sophisticated thermal systems and offer a thorough understanding of the thermal behavior of non-Newtonian hybrid nanofluids.

2. Overview of the Physical Model

Figure 1 illustrates the physical configuration of the domain along with the coordinate system. The governing equations are developed using the Boussinesq approximation, and the flow inside the frame is regarded as laminar and incompressible. A non-Newtonian hybrid nanofluid made of water as the base fluid and a combination of Al_2O_3 and CNT nanoparticles occupies the chamber. subsequently follows that the base fluid and the solid nanoparticles travel at the same speed and stay in thermal balance. Heat transfer within the rectangular cavity is facilitated through two heated diamond shape block inside the enclosure. Figure 1 illustrates how the left and right walls are kept cold while the top and bottom borders are thermally insulated. The solid-state iron particles and base fluid's thermophysical characteristics were used from [47-49].

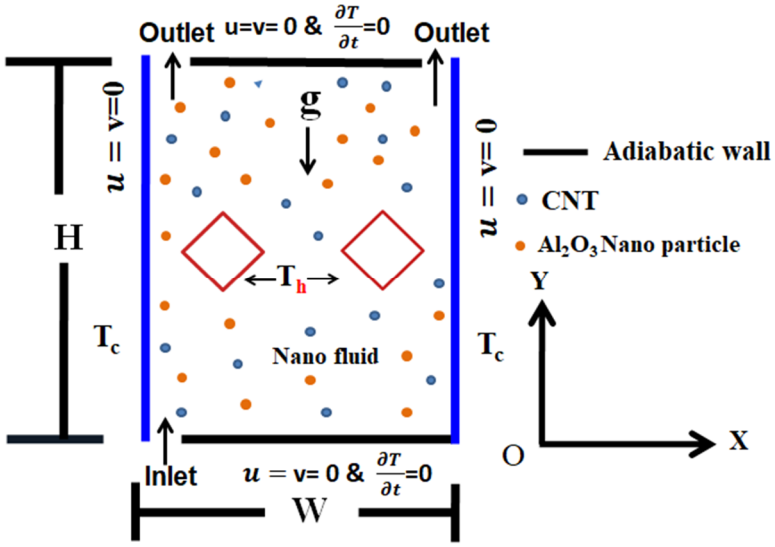

Fig. 1. Schematic diagram of the model considered in this study.

2.1. Features of hybrid nanofluids [50, 51]

Concentration on:

$$\phi = \phi_{Al_2O_3} + \phi_{CNT} \tag{1}$$

The term density (ρ):

$$\rho_{hnf} = \phi_{Al_2O_3}\rho_{Al_2O_3} + \phi_{CNT}\rho_{CNT} + (1-\phi)(\phi_{Al_2O_3} - \phi_{CNT})\rho_f \tag{2}$$

Dynamic Viscosity (μ):

$$\mu_{hnf} = \frac{\mu_f}{1 - 34.87(d_d)^{0.03}\left[(d_{Al_2O_3})^{-0.03}(\phi_{Al_2O_3})^{-1.03} + (d_{CNT})^{-.03}(\phi_{CNT})^{-1.03}\right]}|\gamma|^{n-1} \tag{3}$$

The phrase "heat expansion parameter" refers to thermal volume $(\rho\beta)$:

$$(\rho\beta)_{hnf} = \phi_{Al_2O_3}(\rho\beta)_{Al_2O_3} + \phi_{CNT}(\rho\beta)_{CNT} + (1-\phi)(\phi_{Al_2O_3} - \phi_{CNT})(\rho\beta)_f \tag{4}$$

Thermal volume heat expansion coefficient:

$$(\rho C_p)_{hnf} = \phi_{Al_2O_3}(\rho C_p)_{Al_2O_3} + \phi_{CNT}(\rho C_p)_{CNT} + (1-\phi)(\phi_{Al_2O_3} - \phi_{CNT})(\rho C_p)_f \tag{5}$$

Thermal Conductivity (κ):

$$\kappa_{hnf} = k_f\left((1 + 4.4(Re_r)^{0.4}\,Pr^{0.66})\left(\frac{T_f}{T_{fr}}\right)^{10}(\kappa_f)^{-0.03} \times \left[(\kappa_{Al_2O_3})^{-0.03}(\phi_{Al_2O_3})^{-0.66} + (\kappa_{CNT})^{-0.03}(\phi_{CNT})^{-0.66}\right]\right) \tag{6}$$

The hybrid nanofluid's heat transfer ratio, Re_r, is followed as:

$$Re_r = \frac{\rho_f u_\nu (d_{Al_2O_3} + d_{CNT})}{\mu_f} \tag{7}$$

where,

$$u_\nu = \frac{2k_b T}{\pi\mu_f (d_{Al_2O_3} + d_{CNT})^2} \tag{8}$$

Electrical Conductivity (α):

$$\begin{aligned} \frac{\alpha_{hnf}}{\alpha_{nf}} &= \frac{(1+2\phi_1)\alpha_1 + (1-2\phi_1)\alpha_{nf}}{(1-\varphi_1)\alpha_1 + (1+\phi_1)\alpha_{nf}} \\ \frac{\alpha_{nf}}{\alpha_f} &= \frac{(1+2\phi_2)\alpha_2 + (1-2\phi_2)\alpha_f}{(1-\phi_2)\alpha_2 + (1+\phi_2)\alpha_f} \end{aligned} \tag{9}$$

3. Governing Dimensional Equations

$$\frac{\partial u}{\partial x} + \frac{\partial v}{\partial y} = 0 \tag{10}$$

$$\rho_{hn_f}\left(u\frac{\partial u}{\partial x} + v\frac{\partial v}{\partial y}\right) = -\frac{\partial p}{\partial x} + \frac{\partial}{\partial x}(2\mu_{hnf}u_x) + \frac{\partial}{\partial y}(\mu_{hnf}u_y) + \frac{\partial}{\partial y}(\mu_{hnf}v_x) \tag{11}$$

$$\rho_{hn_f}\left(u\frac{\partial v}{\partial x} + v\frac{\partial v}{\partial y}\right) = -\frac{\partial p}{\partial y} + \frac{\partial}{\partial x}(\mu_{hnf}v_x) + \frac{\partial}{\partial y}(2\mu_{hnf}v_y) + \frac{\partial}{\partial x}(\mu_{hnf}u_y) \tag{12}$$

$$(\rho C_p)_{hnf}\left(u\frac{\partial T}{\partial x} + v\frac{\partial T}{\partial y}\right) = \left[\frac{\partial}{\partial x}(k_{hnf}T_x) + \frac{\partial}{\partial y}(k_{hnf}T_y)\right] \tag{13}$$

3.1. Boundary conditions

$$u = U_{in}, \quad v = 0, \quad T = T_c \tag{14}$$

The two top openings are considered pressure outlets with fully developed flow. Therefore:

$$\frac{\partial u}{\partial n} = 0, \quad \frac{\partial v}{\partial n} = 0, \quad \frac{\partial T}{\partial n} = 0 \tag{15}$$

The vertical walls on the left and right are immobile and kept at the same frigid temperature T_c, so that:

$$u = v = 0, \quad T = T_c \tag{16}$$

The upper wall's solid section is adiabatic and stationary, satisfying:

$$u = v = 0, \quad \frac{\partial T}{\partial n} = 0 \tag{17}$$

Table 1. Thermophysical characteristics of the nanofluid's components [52].

Thermophysical properties	Base fluid (H_2O)	ϕ (Al_2O_3)	ϕ (CNT)
$C_p\ (J/kgK)$	4179	765	425
$\rho\ (kg/m^3)$	997.1	3970	2600
$\kappa\ (Wm^{-1}\kappa^{-1})$	0.613	40	6600
$\beta \times 10^{-5}\ (1/k)$	21	0.85	107

The two diamond-shaped obstacles' surfaces are kept at the same heated temperature, T_h, and remain motionless. Consequently:

$$u = v = 0, \quad T = T_h \tag{18}$$

3.2. Non-dimensional governing equation formula

The following parameters and non-dimensional factors are mentioned:

$$x = \frac{x}{H}, y = \frac{y}{H}, u = \frac{u}{u_0}, t = \frac{tu_0}{H}, p = \frac{p}{p({u_0}^2)}, \theta = \frac{T - T_c}{T_H - T_c}, \nu_f = \frac{\mu_f}{\rho_f}, Pr = \frac{\nu}{\alpha}, Re = \frac{\rho UL}{\mu}, Ri = \frac{Gr}{Re^2}, Gr = \frac{g\beta(T_h - T_c)L^3}{\nu^2} \tag{19}$$

Now making Eqs. (19) to (22) dimensionless construct by applying Eq. (27), then the equation reduces to the equation of continuity:

$$\frac{\partial u}{\partial x} + \frac{\partial v}{\partial y} = 0 \tag{20}$$

u-Momentum Equation:

$$u\frac{\partial u}{\partial x} + v\frac{\partial u}{\partial y} = -\frac{\partial p}{\partial x} + \frac{\rho_f}{\rho_{hnf}}\frac{1}{Re}\left[\frac{\partial}{\partial x}(2\mu_{hnf}u_x) + \frac{\partial}{\partial y}(\mu_{hnf}u_y) + \frac{\partial}{\partial y}(\mu_{hnf}v_x)\right] \tag{21}$$

v-Momentum Equation:

$$u\frac{\partial v}{\partial x} + v\frac{\partial v}{\partial y} = -\frac{\partial p}{\partial y} + \frac{\rho_f}{\rho_{hnf}}\frac{1}{Re}\left[\frac{\partial}{\partial x}(\mu_{hnf}v_x) + \frac{\partial}{\partial y}(2\mu_{hnf}v_y) + \frac{\partial}{\partial x}(\mu_{hnf}u_y)\right] + Ri\frac{(\rho\beta)_{nf}}{\rho_{nf}\beta_f}\theta \tag{22}$$

Energy Equation:

$$u\frac{\partial \theta}{\partial x} + v\frac{\partial \theta}{\partial y} = \frac{(\rho C_p)_f}{(\rho C_p)_{nf}}\frac{1}{RePr}\left[\frac{\partial}{\partial x}\left(\frac{\kappa_{hnf}}{\kappa_f}\theta_x\right) + \frac{\partial}{\partial y}\left(\frac{\kappa_{hnf}}{\kappa_f}\theta_y\right)\right] \tag{23}$$

3.3. Thermophysical properties

The volume fraction of nanoparticles in this investigation, represented by ϕ, has been taken into account. Specifically, the volume fraction is expressed by ϕ of alumina (Al_2O_3) and carbon nanotubes (CNT), while water serves as the base fluid within the enclosure. The base fluid's and the nanoparticles' thermophysical characteristics (Al_2O_3 and CNT) are summarized in Table 1.

4. Numerical Methods

The Galerkin weighted residual approach and the finite element approach, or FEM, are used in this study. Temperature and velocity are interpolated using quadratic functions, while pressure is interpolated using linear functions. The fluid domain is discretized into separated triangular parts. Estimates of dependent factors in coordinates of local features, and the resulting global nonlinear algebraic equations are solved using minimum errors numerical technique. Convergence is achieved when the difference between successive iterations for all variables falls below a prescribed tolerance, δ [53, 54].

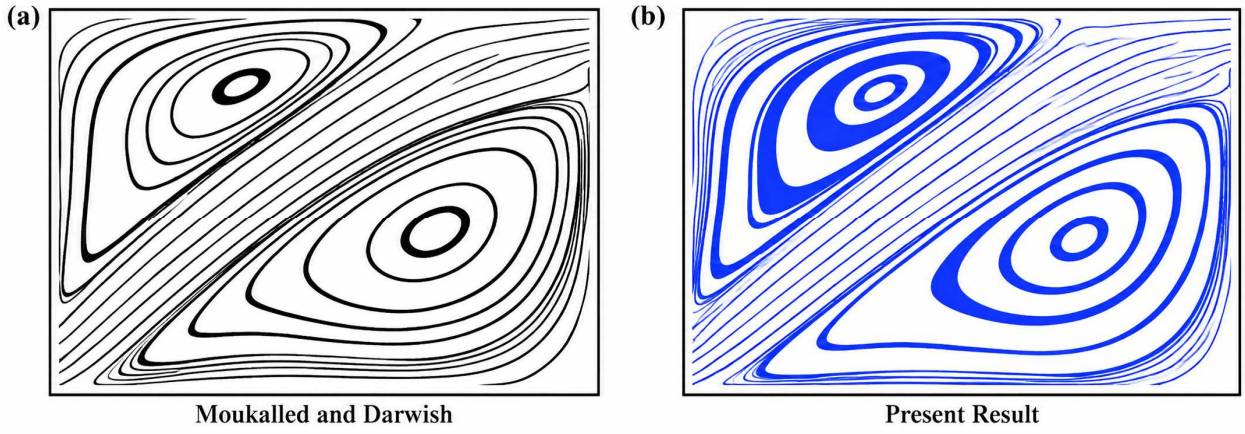

Fig. 2. A review of the (a) existing streamlines with (b) the result of Moukalled and Darwish [55] where Re = 500.

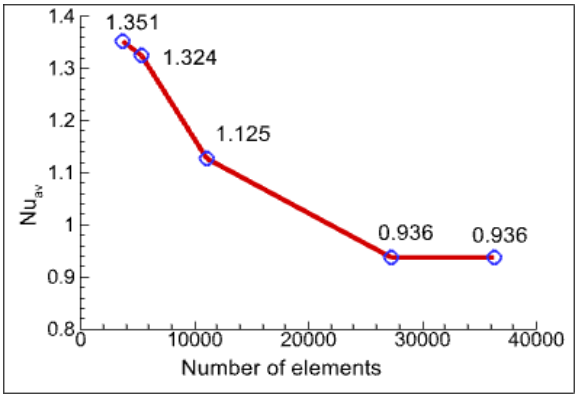

Fig. 3. Grid independence test for this finite element method.

5. Quantitative Code Validation for the Nanofluids

Figure 2 provides a qualitative analysis of the streamline patterns with the results reported by Moukalled and Darwish [55], who suggested a brand-new class of high-resolution, streamline-based patterns. Their study considered flow at a high Reynolds number (Re = 500) is a square space featuring ports for the inlet and outflow. The boundary walls were kept at low temperatures at the input and outflow, and they were thermally adiabatic. Figure 2(a) illustrates the streamline distribution from Moukalled and Darwish [55], whereas Fig. 2(b) depicts the present numerical results. A close similarity between the two streamline patterns is observed, indicating good agreement with the benchmark solution and reinforcing the validity of the present numerical approach.

5.1. Grid independence test

For the grid independence test, apply the following characteristic values: For this non-Newtonian force convective nanofluid flow model, the optimal number of parts for this FEM is determined to be Re = 300, Ri = 6.0, ϕ = 0.02, Pr = 6.2, and n = 0.6. For the sensitivity analysis of the mesh construction method, the ideal Nu_{av} value is selected. With the numbers 3617, 5330, 11072, 27306, and 36284, respectively, five sets of triangular elements make up the domain. Figure 3 shows that the Nu_{av} values for the triangle portions 27306 and 36284 are almost comparable. The 27306 triangle elements are therefore ideal for completing and characterizing the design.

5.2. Effect of Re on streamlines and isotherms

The result of the Reynolds number (Re) on the streamline distributions for ϕ = 0.02, n = 0.6, and Ri = 1.0 is displayed in Figs. 4(a–d). With a dominant primary vortex and minor secondary vortices encircling the heated cylinders, the flow is comparatively feeble at Re = 50, suggesting that viscous forces have a major impact on the flow. Primary circulation becomes stronger and spreads farther inside the enclosure as the Reynolds number climbs to 100, while the secondary vortices become more noticeable. Streamline density rises in the middle region and around the cylinders at Re = 200, indicating increased fluid mixing and stronger inertial effects. Higher flow velocity and more intense recirculation are shown by the streamlines' extreme contraction along the main flow channel and around the heated cylinders for Re = 400. As a result, boosting the Reynolds number promotes convective transport across the enclosure, promotes fluid circulation, and reduces viscous effects. The isotherm distributions for various Reynolds numbers for ϕ = 0.02, n = 0.6, and Ri = 1.0 are presented in Figs. 4(e-h). The isotherms around the heated cylinders are almost symmetrical at Re = 50, indicating that conduction dominates heat transfer with comparatively little convective transport. A moderate temperature gradient is reflected in the smooth thermal contours that progressively extend toward the cold wall.

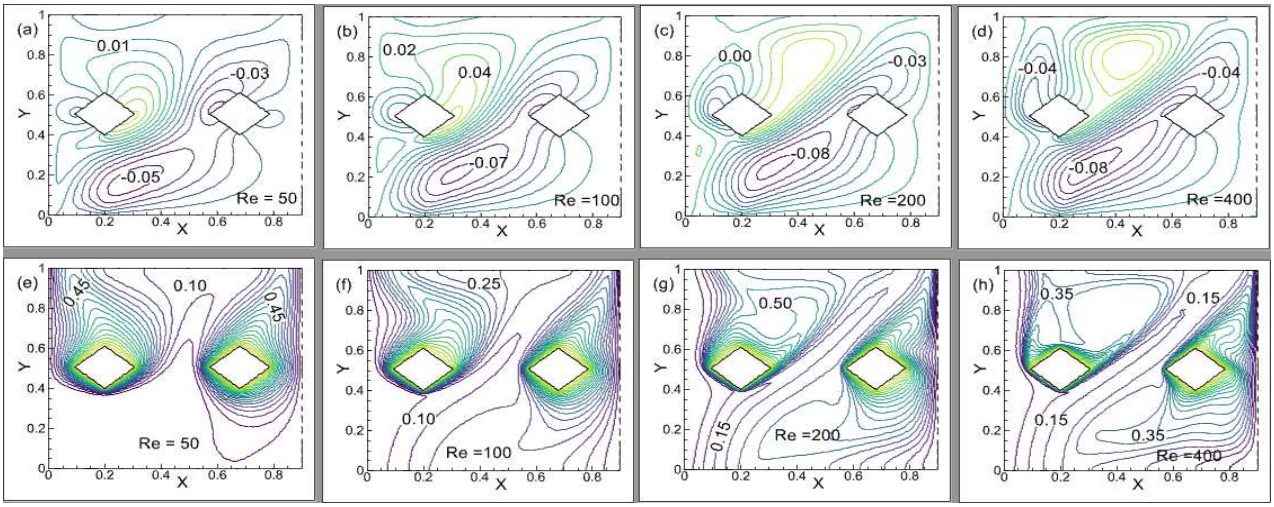

Fig. 4. (a-d) Streamlines and (e-h) Isotherms for Re = 50, Re = 100, Re = 200 and Re = 400 when ϕ = 0.02, n = 0.6 and Ri = 1.0.

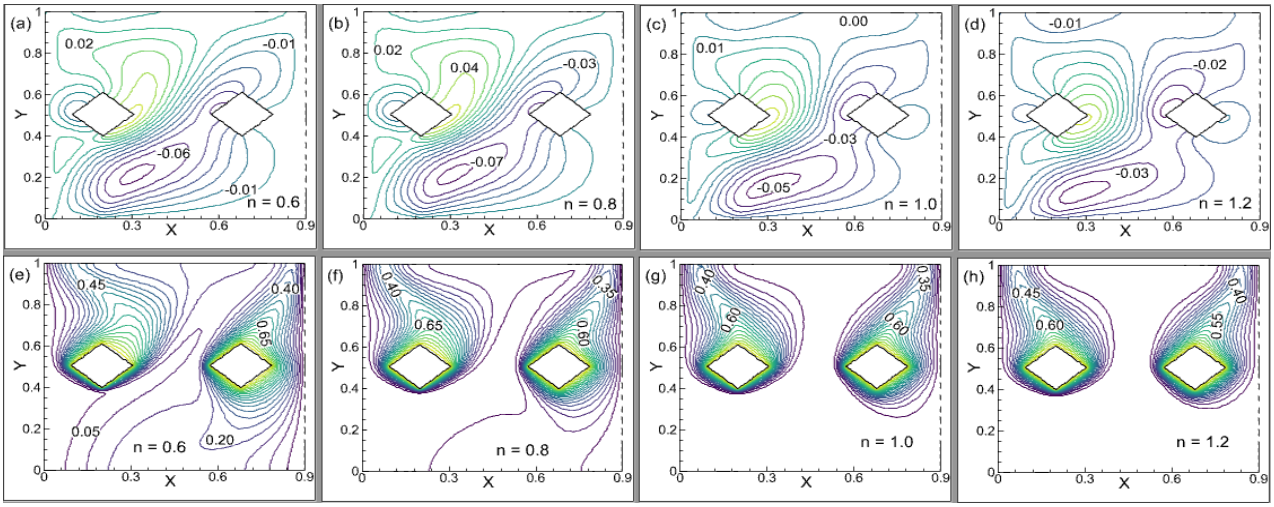

Fig. 5. (a-d) Streamlines and (e-h) Isotherms for n = 0.6, n = 0.8, n = 1.0, and n = 1.2 when ϕ = 0.02, Ri = 1.0 and Re = 10.

Stronger fluid motion causes the isotherms to become more warped and stretched along the flow direction as Re rises to 100. Increased convective heat transfer is indicated by the thinner thermal boundary layers surrounding the heated cylinders. More effective thermal mixing within the enclosure appears at Re = 200, where the isotherms are further squeezed close to the heated surfaces and transported toward the outlet region. Thermal plumes extend farther into the cavity at Re = 400, and the isotherms show the most distortion and clustering around the heated cylinders. This result demonstrates that raising the Reynolds number enhances the enclosure's overall heat transfer performance by strengthening forced convection and decreasing the thickness of the thermal boundary layer.

5.3. Effect of power-law index n on streamlines and isotherms

The streamline distributions for various power-law indices (n) at ϕ = 0.02, Re = 100, and Ri = 1.0 are presented in Figs. 5(a–d). Large primary recirculation cells that occupy the majority of the enclosure and densely packed streamlines surrounding the heated cylinders are characteristic of the shear-thinning fluid, which displays the strongest fluid motion at n = 0.6. Because of the decreased apparent viscosity, this behavior suggests improved circulation and mixing. Streamline density encircling the cylinders drops, and the principal vortices become somewhat weaker as the power-law index rises to n = 0.8, indicating a steady decline in flow intensity. Recirculation zones become more symmetric and somewhat weaker at n = 1.0, which corresponds to the Newtonian fluid, and the vortex cores move slightly away from the heated cylinders. The streamlines become more widely dispersed, and vortex intensity dramatically falls when the power-law index is further increased to n = 1.2, implying inhibited fluid circulation brought on by the shear-thickening fluid's higher apparent viscosity. In general, raising the power-law index results in a less efficient convective transport mechanism by weakening recirculation intensity and decreasing fluid mixing within the enclosure. The isotherm distributions for different power-law indices (n) for ϕ = 0.02, Re = 100, and Ri = 1.0 are displayed in Figs. 5(e–h). Strong convective heat transfer associated with the fluid's shear-thinning behavior is demonstrated by the isotherms' extreme distortion and deep extension into the enclosure at n = 0.6. Heat transfer is facilitated by the comparatively small thermal boundary layers encircling the heated cylinders. Isotherms around the heated cylinders become less distorted and more densely packed as the power-law index rises to n = 0.8, indicating a steady decline in convective mixing brought on by an upward trend in apparent viscosity. The thermal plumes are less noticeable, and the thermal contours become smoother and more symmetric in the Newtonian case (n = 1.0), reflecting a more balanced conduction-convection mechanism. Thick thermal boundary layers and weaker thermal mixing emerge from the isotherms' close proximity to the heated cylinders at n = 1.2 and their limited penetration into the surrounding fluid. As a result, raising the power-law index reduces the enclosure's total heat transfer performance by inhibiting convective heat transport and shifting the heat transfer mechanism toward conduction.

5.4. Effect of Ri on streamlines and isotherms

The result of the Richardson number (Ri) on the streamline distributions at Re = 100, n = 0.6, and ϕ = 0.02 is displayed in Figs. 6(a-d). The majority of the enclosure is consumed by a dominant primary vortex at Ri = 1.0, with minor secondary vortices surrounding the heated cylinders, emphasizing the combined effect of forced and natural convection. The secondary vortices become more noticeable as Ri rises to 2.0, while the primary circulation gets stronger and reaches farther into the upper part of the hollow. The streamline density surrounding the heated cylinders rises at Ri = 4.0, indicating better fluid mixing and more buoyancy-induced circulation. The primary vortex grows larger, and the recirculation zones close to the heated cylinders intensify at Ri = 6.0. According to these outcomes, buoyancy effects are augmented by boosting the Richardson number, which leads to improved convective transport and fluid circulation inside the enclosure. The isotherm distributions based on different Richardson numbers for Re = 100, n = 0.6, and ϕ = 0.02 are shown in Figs. 6(e-h). The isotherms are concentrated around the heated cylinders and are relatively smooth at Ri = 1.0, suggesting convective heat transfer. The growing effect of buoyancy-driven flow causes the thermal contours to become more distorted and travel farther into the enclosure as Ri rises to 2.0. Isotherms show increased penetration into the fluid domain and are compressed close to the heated surfaces for Ri = 4.0, indicating improved thermal mixing. At Ri = 6.0, the thermal boundary layers thin and the thermal outlines become significantly deformed, shifting away from the heated cylinders. This result indicates that raising the Richardson number boosts thermal mixing, promotes natural convection, and raises the enclosure's overall heat transfer efficiency.

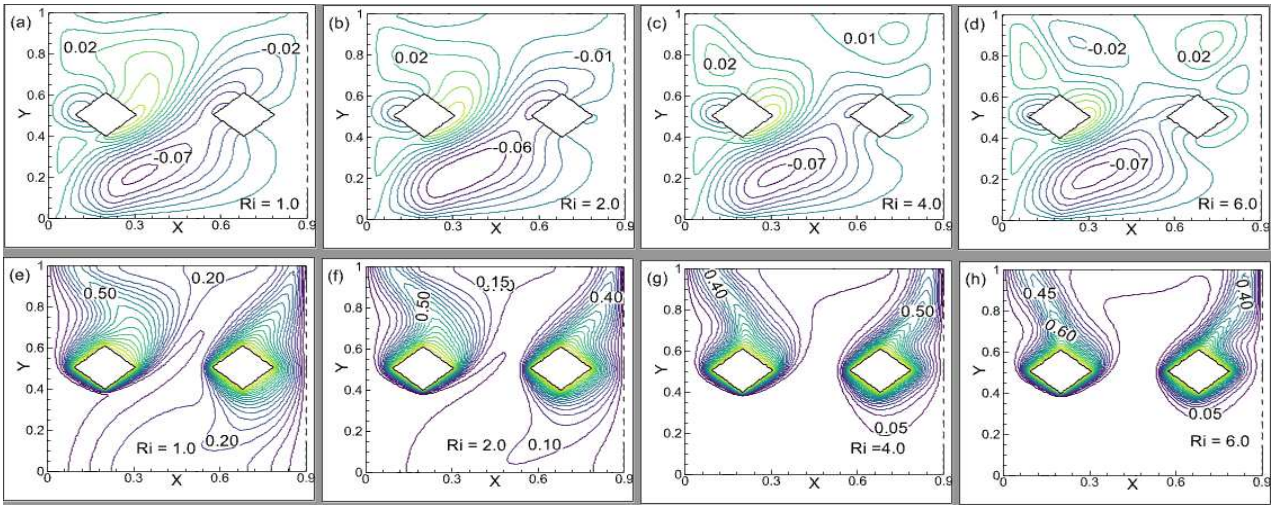

Fig. 6. Streamlines (a-d) and temperatures (e-h) for Ri = 1.0, 2.0, 4.0 and 6.0 while for fixed Re = 100, n = 0.6 and ϕ = 0.02.

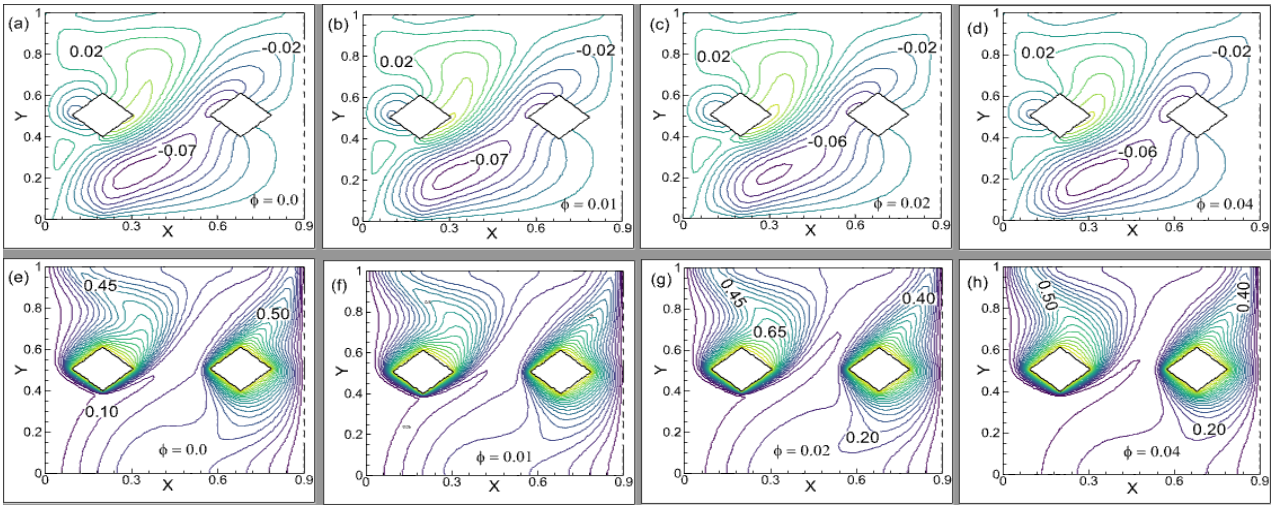

Fig. 7. (a-d) Streamlines, and (e-h) Isotherms for ϕ = 0.00, 0.01, 0.02, and 0.04 when Ri = 1.0, Re = 100, and n = 0.6.

5.5. Effect of ϕ on streamlines and isotherms

Figures 7(a–d) demonstrate how the streamline distributions for Ri = 1.0, Re = 100, and n = 0.6 are impacted by the nanoparticle volume fraction (ϕ). The flow is characterized by minor secondary vortices surrounding the heated cylinders and a dominant primary vortex that occupies the majority of the enclosure for the base fluid (ϕ = 0.00). The streamline density rises, and the secondary vortices become more noticeable when the nanoparticle volume fraction rises to ϕ = 0.01 and 0.02, suggesting improved fluid circulation and stronger recirculation around the heated cylinders. The primary vortex gets a little stronger at the maximum volume fraction, ϕ = 0.04, and the streamlines are closer together close to the heated surfaces, indicating better fluid mixing and momentum conveyance. All things considered, enhancing the concentration of nanoparticles improves the convective flow and circulation intensity within the enclosure. The corresponding isotherm distributions for varying nanoparticle volume fractions can be seen in Figs. 7(e-h). Moderate heat transfer is indicated by the isotherms' smooth distribution around the heated cylinders with relatively thick thermal boundary layers at ϕ = 0.00. The thermal contours become more compressed nearer to the heated cylinders and extend deeper into the enclosure when the nanoparticle volume fraction climbs to ϕ = 0.01 and 0.02. This indicates improved thermal transfer because of the nanofluid's improved effective thermal conductivity. Stronger convective heat transfer and thinner thermal boundary layers are demonstrated by the isotherms' greater distortion along the flow direction and denser packing around the heated surfaces at ϕ = 0.04. As an outcome, boosting the nanoparticle volume percentage improves thermal mixing and the enclosure's overall heat transmission efficiency.

5.6. Velocity Variation for Re, Ri, n, and ϕ

Figure 8(a) depicts the horizontal velocity components along y = 0.7 for different Reynolds numbers (Re). As Re increases, the velocity profiles propagate with higher magnitudes from the origin (x = 0). All profiles show positive velocity values around x = 0.3, followed by negative values near x = 0.6, and eventually converge at the downstream end. The profile corresponding to Re = 50 exhibits the lowest velocity magnitude, while a clear increasing trend is observed as Re rises from 50 to 300. Interestingly, although the positive peak decreases at Re = 400, it displays the highest negative velocity magnitude among all cases. Figure 8(b) reveals the impact of the Richardson number (Ri) on the velocity profiles. All curves start from zero and merge at the endpoint. As Ri increases, velocity magnitudes also increase, indicating the strengthening of buoyancy effects. Power-law index (n) and its effects on the velocity distribution are shown in Fig. 8(c). The velocity profiles exhibit a consistent increasing trend as n

decreases, with the highest magnitude observed for n = 0.6, representing shear-thinning behavior. Finally, Fig. 8(d) depicts the velocity profiles for various nanoparticle volume fractions (ϕ). The profiles remain closely aligned, showing minimal deviations as ϕ varies, which indicates that the impact of nanoparticle levels on velocity distribution is relatively insignificant.

5.7. Distribution of temperatures for Re, Ri, n, and ϕ

Figure 9(a) shows the thermal distribution corresponding to different Reynolds numbers (Re). The velocity profiles originate from x = 1 and converge again at the same position. For Re = 50, the temperature distribution exhibits a parabolic shape. With increasing Re, the peak amplitude of the temperature profile gradually increases, and the curves corresponding to Re = 100, 200, and 400 intersect at x = 0.4. Notably, higher temperature magnitudes are observed around x = 0.6, indicating that thermal performance improves with increasing Re. Figure 9(b) further shows how the Richardson number (Ri) affects the temperature distribution for fixed parameters Re = 100, n = 0.6, and ϕ = 0.04. Temperature magnitudes increase consistently with Ri in all considered cases. The maximum temperature magnitude is observed at x = 0.6 for Ri = 6.0, highlighting the significant impact of buoyancy forces on the heated region. Figure 9(c) shows how the power-law index (n) affects the temperature distribution. As n increases, the peak amplitude of all temperature profiles decreases. The maximum temperature amplitude occurs at x = 0.6 for the shear-thinning fluid with n = 0.6. Figure 9(d) presents the impact of the volume fraction (ϕ) of nanoparticles on the temperature distribution to identify variations in the thermal profile. The peak amplitudes for different ϕ values are clearly observed at x = 0.6. Only slight variations are noted in the temperature curves for different nanoparticle concentrations, indicating a relatively moderate effect of ϕ on the overall temperature distribution.

5.8. Effect on Nusselt number

Figures 10(a–c) depict the variation of the fins' average Nusselt number in relation to heat transfer as the nanoparticle volume fraction, ϕ, changes. Figure 10(a) shows that at lower ϕ, the heat transfer rate increases with Reynolds number (Re). As ϕ increases, the convective heat transfer rate gradually decreases. It is also evident from Fig. 10(a) that the average Nusselt number exhibits similar trends for Re = 150 to 200. In contrast, convective heat transfer is improved at larger Reynolds numbers for all values. Figure 10(b) illustrates the variation of the average Nusselt number with respect to both the nanoparticle volume fraction, ϕ, and the Richardson number, Ri. For ϕ = 0.0, the heat transfer rate remains relatively steady with minor fluctuations. As ϕ increases, convective heat transfer is enhanced up to ϕ = 0.04. For ϕ = 0.06, the curve starts at a comparatively lower level but eventually aligns with the peak values observed at ϕ = 0.04.

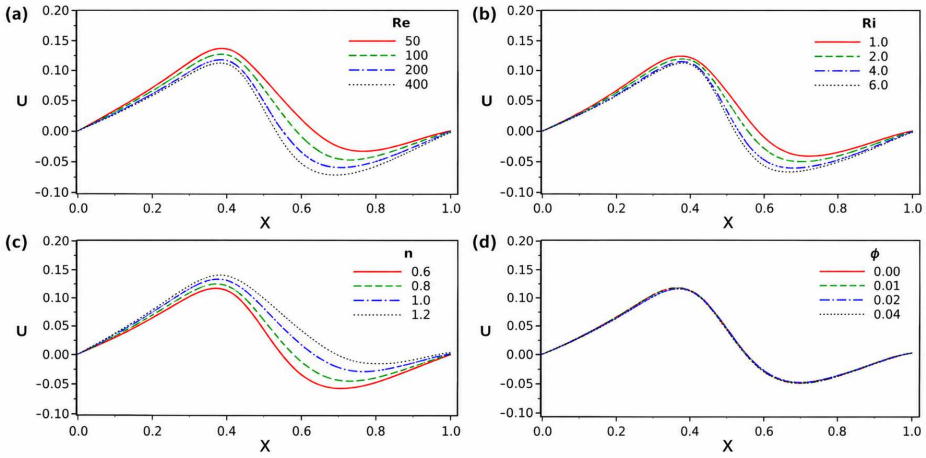

Fig. 8. Velocity profiles at the point y = 0.7 (a) for Re = 50, 100, 200, and 400, with fixed Ri = 1.0, ϕ = 0.02, and n = 0.6; (b) for Ri = 1.0, 2.0, 4.0, and 6.0, with fixed Re = 100, ϕ = 0.02, and n = 0.6; (c) for n = 0.6, 0.8, 1.0, and 1.2, with fixed Ri = 1.0, ϕ = 0.02 and Re = 100; and (d) for ϕ = 0.0, 0.01, 0.02, and 0.04, with fixed Ri = 1.0, n = 0.6, and Re = 100.

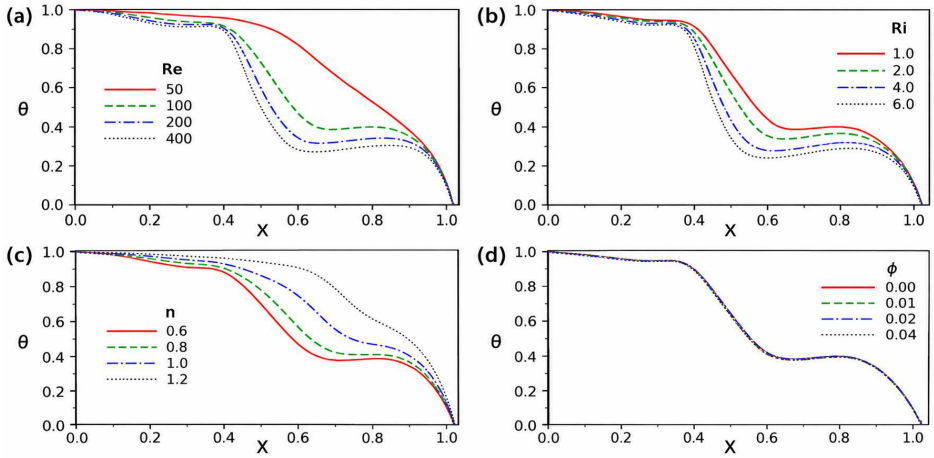

Fig. 9. Temperature profiles at the point y = 0.7: (a) for Re = 50, 100, 200, and 400, with fixed Ri = 1.0, ϕ = 0.02, and n = 0.6; (b) for Ri = 1.0, 2.0, 4.0, and 6.0, with fixed (Re = 100), ϕ = 0.02, and n = 0.6; (c) for n = 0.6, 0.8, 1.0, and 1.2, with fixed Ri = 1.0, ϕ = 0.02, and Re = 100; and (d) for ϕ = 0.0, 0.01, 0.02, and 0.04, with fixed Ri = 1.0, n = 0.6, and Re = 100.

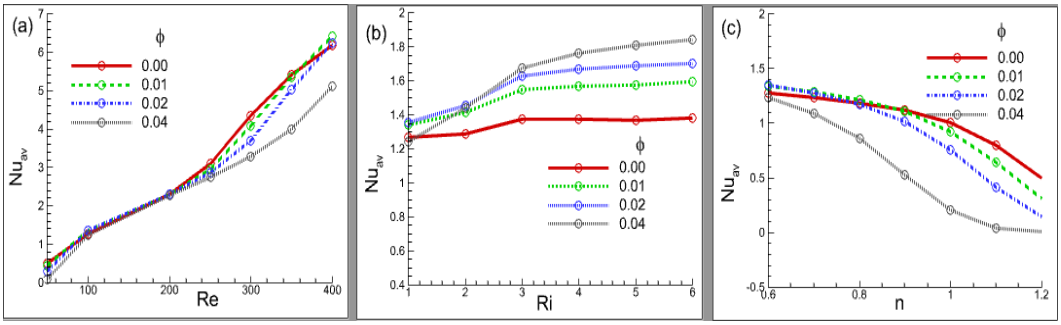

Fig. 10. Variation of Nu_{av} for (a) Re = 50, 100, 200, and 400; (b) Ri = 1.0, 2.0, 4.0, and 6.0; (c) n = 0.6, 0.8, 1.0, and 1.2.

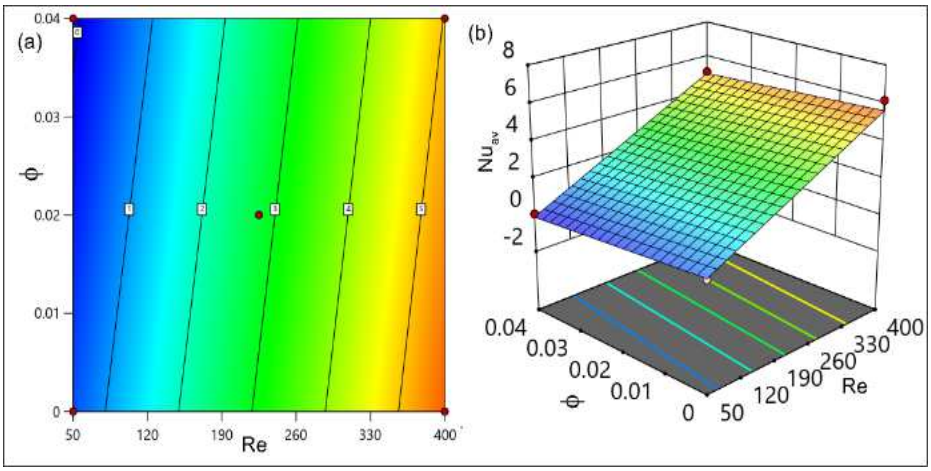

Fig. 11. Effect of Re and ϕ on Nu_{av}: (a) 2D sight, (b) 3D sight.

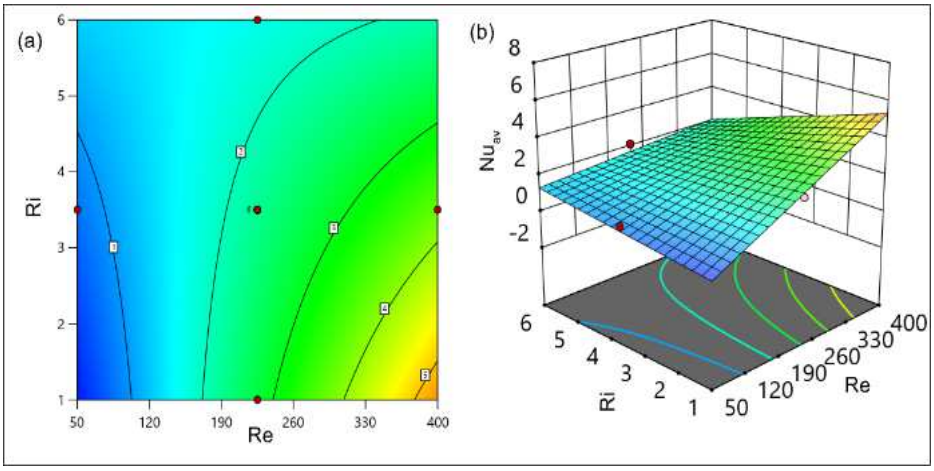

Fig. 12. Effect of Re and Ri on Nu_{av}: (a) 2D sight, (b) 3D sight.

Overall, the average Nusselt number increases with Ri for every volume fraction of nanoparticles, as clearly presented in Fig. 10(b). Fluctuations of the mean Nusselt number with respect to the power-law index, n, and the volume fraction of nanoparticles, ϕ, are shown in Fig. 10(c). The rate of heat transmission falls notably for ϕ = 0 as n increases from 0.9 to 1.2. When ϕ increases from 0.02 to 0.06, additionally, convective heat transfer decreases, following a similar trend for n values between 1.1 and 1.2. For ϕ = 0.06, the average Nusselt number remains nearly constant as n increases from 1.0 to 1.2. Overall, as Fig. 10(c) makes evident, the average Nusselt number tends to decrease with rising n for all ϕ, with the exception of the ϕ = 0.06 case in the range n = 1.0 to 1.2. Nu_{av} for Al_2O_3, CNT, and both combined nanofluids are shown in Figs. 10(a) and 10(b) for ϕ = 0.02, with fixed values of Re = 300 and n = 0.6. The hybrid nanofluid exhibits higher values than the individual nanofluids, as can be seen in both figures.

5.9. Response surface analysis

Response surface methodology (RSM) has become a widely adopted statistical tool for simulating multivariate systems, as the input parameters significantly influence the resulting physical responses [57]. Recent studies [58, 55] have successfully employed RSM-based models to examine the features of evaporative heat transfer. Figures 11(a-b) depict the two- and three-dimensional response surfaces of the average Nusselt number Nu_{av} as functions of Re, Ri, and ϕ. As shown in Figs. 11(a-b), Nu_{av} increases with higher Re and ϕ, demonstrating the enhancement of convective heat transfer at elevated flow inertia and nanoparticle concentration.

Table 2. ANOVA results for F-value and P-value.

Source	Sum of squares	df	Mean square	F-value	p-value	Interpretation
Model	34.48	6	5.75	47.31	< 0.0001	Significant
A–Re	21.79	1	21.79	179.42	< 0.0001	Significant
B–Ri	2.77	1	2.77	22.83	0.0004	Significant
C–ϕ	0.0005	1	0.0005	0.0043	0.9484	Not significant
AB	9.15	1	9.15	75.34	< 0.0001	Significant
AC	0.0011	1	0.0011	0.0090	0.9259	Not significant
BC	0.7622	1	0.7622	6.27	0.0263	Significant
Residual	1.58	13	0.1215			
Lack of fit	1.58	8	0.1974			
Pure error	0.0000	5	0.0000			
Core total	36.06	19				

Figures 12(a-b) further illustrate the coupled influence of Re and Ri on Nu_{av}, where the contour intensity and gradient become more pronounced with increasing parameter values. Similarly, Figs. 12(a-b) reveal a distinct nonlinear variation of Nu_{av} with Ri and ϕ, where the contour profiles evolve from circular to elongated shapes, indicating strengthened thermal transport. Finally, Figs. 13(a-b) present the RSM response surfaces for Nu_{av} as functions of Ri and ϕ, showing excellent agreement between the RSM predictions and numerical results, thereby confirming the robustness of the developed model.

6. ANOVA Discussion

Analysis of variance (ANOVA) was used to assess the created response surface model's statistical significance; the findings are displayed in the table. With an F-value of 47.31 and a p-value of less than 0.0001, the model as a whole is highly significant. The created model offers a statistically significant depiction of the link between the governing parameters and the average Nusselt number because the p-value is significantly less than the significance level of 0.05.

Reynolds number Re has a maximum F-value of 179.42 with ($p < 0.0001$) among the individual model terms, indicating a highly significant contribution to the variation. The Richardson number Ri is similarly statistically significant, with an F-value of 22.83 and a p-value of 0.0004. On the other hand, the nanoparticle volume fraction's individual effect is statistically insignificant ($F = 0.0043$, $p = 0.9484$). Re and Ri's interaction is significant ($F = 75.34$, $p < 0.0001$), indicating that their combined effect significantly impacts the heat-transfer response. While the interaction is significant ($F = 6.27$, $p = 0.0263$), it is statistically insignificant ($F = 0.0090$, $p = 0.9259$). Overall, the fitted response surface model captures a statistically significant relationship between the selected input parameters, as confirmed by the highly significant model F-value. The resulting model's suitability for characterizing the numerical heat-transfer data is further supported by the statistical significance of the key main and interaction elements.

6.1. Assessment and review of models

Based on the identical experimental dataset (N = 20), statistical metrics such as the Coefficient of Determination (R^2), Root Mean Squared Error (RMSE), and Mean Absolute Error (MAE) were computed to assess and compare the predictive abilities of the Artificial Neural Network (ANN) and Response Surface Methodology (RSM) models. The table summarizes the performance results.

7. Artificial Neural Networks for Data Interpretation

Artificial intelligence (AI) is a potent computational tool for resolving challenging engineering issues. Artificial neural networks (ANNs) are widely used among its different methodologies because they can immediately learn highly nonlinear relationships from data without needing explicit mathematical definitions. ANNs, which draw inspiration from the human brain, can identify hidden patterns, extract significant features, and produce precise forecasts with little assistance from humans.

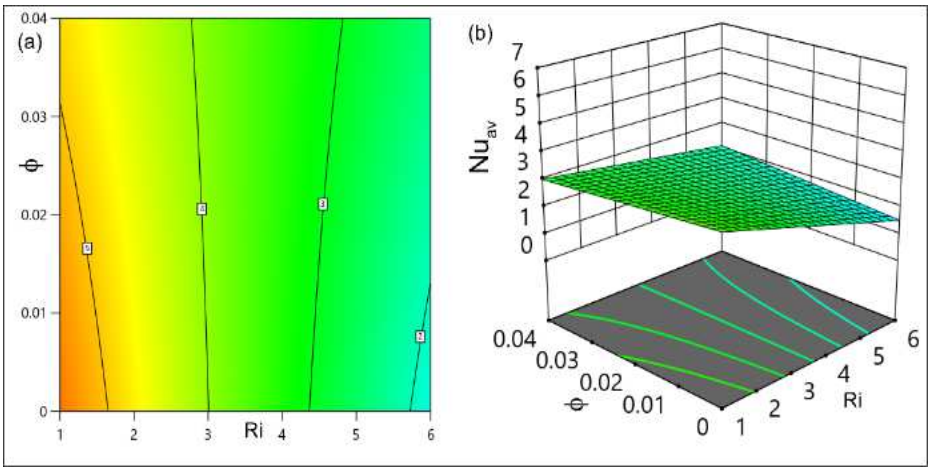

Fig. 13. Effect of Ri and ϕ on Nu_{av}: (a) 2D sight, (b) 3D sight.

Table 3. ANN and RSM models' relative results are shown.

Performance Metric	ANN Model	RSM Model
Coefficient of Determination R^2	0.7410	0.8845
Root Mean Squared Error (RMSE)	0.7250	0.4828
Mean Absolute Error (MAE)	0.2783	0.3702

As a result, ANNs have been effectively used in many engineering domains, such as thermal engineering, image processing, pattern recognition, handwriting recognition, weather forecasting, and military applications [59, 60]. An input layer, one or more hidden layers, and an output layer coupled by weighted neurons assemble an artificial neural network. While the hidden layers employ nonlinear activation functions to extract representative features from the input data, the input layer receives the independent variables. Lastly, the anticipated reaction is generated by the output layer. The ANN effectively captures the intricate nonlinear interactions between the input variables and the output response because of its multilayer construction. The general design of the suggested ANN model is shown in Fig. 14(a). An ANN model for predicting the average Nusselt number (Nu_{av}) was developed in this work using three input parameters: the Reynolds number (Re), the Richardson number (Ri), and the nanoparticle volume fraction (ϕ), as shown in Table 3. Twenty numerical datasets were produced by the CFD simulations, of which 85% (20) used labeled CFD data, and a supervised learning approach was used to train the ANN model. It consists of four hidden layers in the network, each with 128, 64, 32, and 16 neurons. To improve the network's capacity for nonlinear learning, each hidden layer uses the Rectified Linear Unit (Re_{LU}) activation function. To reduce prediction error, the back-propagation technique was used to modify the network weights iteratively. The average Nusselt number was predicted by a single neuron in the output layer. The ANN-predicted values and the matching CFD-calculated average Nusselt numbers are compared in Fig. 15(a). Excellent agreement between the ANN predictions and the numerical findings is demonstrated by the distribution of most prediction points near the fitted regression line. The general correlation supports the created ANN model's dependability and prediction abilities, despite a few samples showing comparatively greater variances. Figure 15(b) illustrates the mean squared error (MSE) for each testing sample. Only a tiny number of examples have relatively larger MSE values, but the majority of samples show very minor prediction errors. The small number of training samples is the primary cause of these disparities. However, for the examined operational conditions, the ANN model offers adequate prediction accuracy. The training and validation loss curves across 500 epochs appear in Fig. 16. The ANN successfully learns the nonlinear relationship between the input parameters (Re, Ri, and ϕ) and the average Nusselt number, as both curves rapidly decline during the first training phase. While the validation loss stabilizes at a nearly constant value after about 120 epochs, the training loss approaches practically zero after about 80-100 epochs. Stable convergence and adequate generalization of the suggested ANN model are indicated by the lack of noticeable oscillations or divergence between the two curves.

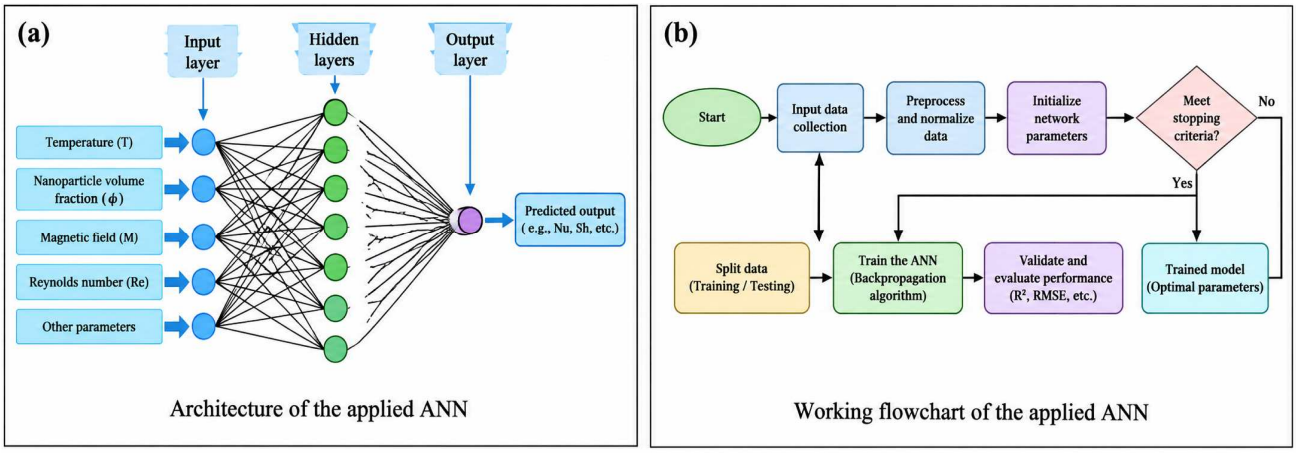

Fig. 14. (a) Architecture of the applied ANN, (b) working flowchart of the applied ANN.

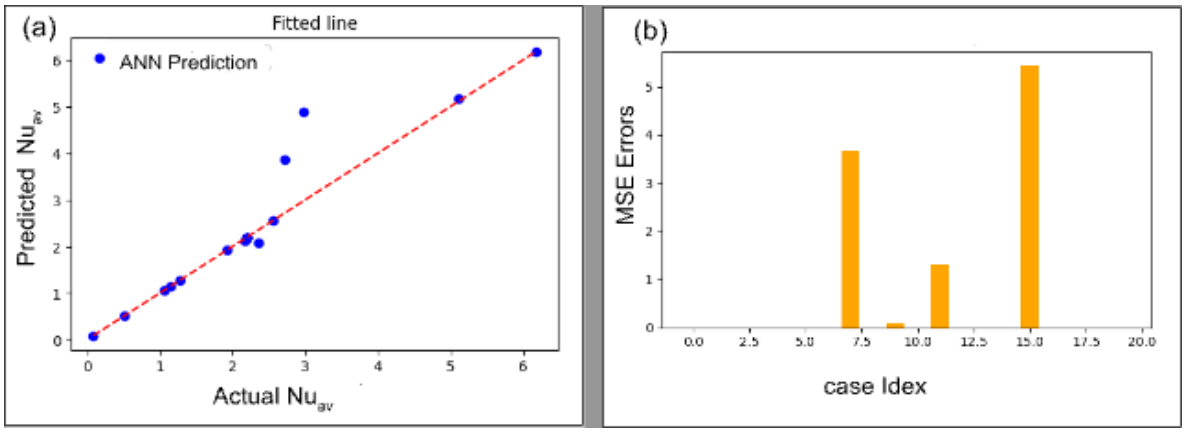

Fig. 15. (a) Predicted versus actual values and, (b) MSE error per case.

Table 4. Comparison between actual and ANN-predicted average Nusselt number.

Re	Ri	ϕ	Actual Nu	Predicted Nu	MSE per Case
225	1.0	0.02	2.551500	2.551500	6.726623×10^{-15}
50	6.0	0.00	1.149500	1.149500	1.537046×10^{-16}
225	3.5	0.00	1.927100	1.927100	3.230671×10^{-15}
225	3.5	0.02	2.195800	2.195800	4.355243×10^{-15}
225	3.5	0.02	2.195800	2.195800	4.355243×10^{-15}
225	6.0	0.02	2.163700	2.129405	1.176129×10^{-3}
400	1.0	0.04	5.111400	5.157416	2.117460×10^{-3}
400	3.5	0.02	2.970800	4.882908	3.656156
225	3.5	0.02	2.195800	2.195800	4.355243×10^{-15}
225	3.5	0.04	2.360100	2.068905	8.479446×10^{-2}
225	3.5	0.02	2.195800	2.195800	4.355243×10^{-15}
400	6.0	0.04	2.713300	3.856715	1.307399
50	1.0	0.00	0.503990	0.503990	2.996567×10^{-17}
400	1.0	0.00	6.175100	6.175100	2.258981×10^{-14}
225	3.5	0.02	2.195800	2.195800	4.355243×10^{-15}
400	6.0	0.00	1.855700	4.189229	5.445358
50	3.5	0.02	1.056100	1.056100	1.181979×10^{-16}
50	6.0	0.04	1.273700	1.273700	1.309672×10^{-18}
225	3.5	0.02	2.195800	2.195800	2.973014×10^{-14}
50	1.0	0.04	0.080202	0.080202	2.712594×10^{-18}

Table 5. Hyperparameters table.

Parameter	Specification
ANN inputs	Re, Ri, and ϕ
ANN output	Average Nussle number, Nu_{av}
Number of hidden layers	4
Neurons in hidden layers	128–64–32–16
Hidden-layer activation function	Re_{LU}
Output-layer activation function	Linear
Training algorithm	Back propagation
Loss function	Mean Squared Error (MSE)
Maximum number of epochs	500
Stopping criterion	Maximum of 500 epochs / convergence of validation loss
Training data	CFD-generated numerical data
Number of CFD samples	20
Data normalization	Min–max normalization [0,1]

The somewhat greater validation loss compared with the training loss can be attributed primarily to the very small dataset of only 20 samples; however, the regression and MSE evaluations demonstrate that the constructed ANN provided reasonable prediction accuracy within the investigated parameter range, although relatively larger errors were observed for some cases. The outlined ANN model provides an efficient alternative to computationally intensive CFD simulations for estimating the average Nusselt number within the explored range of Reynolds number (Re), Richardson number (Ri), and flow nanoparticle volume fraction (ϕ). Once trained, the model can rapidly estimate thermal performance for novel combinations of these input parameters, therefore drastically decreasing computing cost while maintaining satisfactory prediction accuracy. Furthermore, the established ANN framework can be extended to various non-Newtonian fluid flow and heat transfer problems for engineering design and optimization.

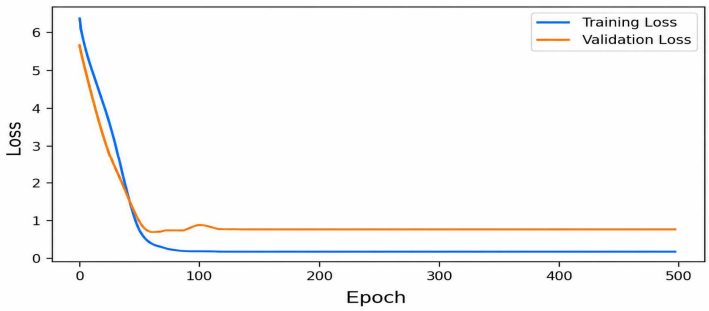

Fig. 16. Loss curve for loss vs. epochs.

8. Data Normalization Equations

A commonly used method is min–max normalization, which scales the data to the range [0, 1]. The normalized value is calcul ated as:

$$X_{norm} = \frac{X - X_{min}}{X_{max} - X_{min}} \tag{24}$$

where X represents the original value, while X_{min} and X_{max} denote the minimum and maximum values of the corresponding variable, respectively. For the developed ANN model, the input variables are Re, Ri, and ϕ, while the output is the average Nusselt number, Nu_{av}. Thus, the normalized input variables are expressed as:

$$Re_{norm} = \frac{Re - Re_{min}}{Re_{max} - Re_{min}} \tag{25}$$

$$Ri_{norm} = \frac{Ri - Ri_{min}}{Ri_{max} - Ri_{min}} \tag{26}$$

$$\phi_{norm} = \frac{\phi - \phi_{min}}{\phi_{max} - \phi_{min}} \tag{27}$$

while the normalized output is given by:

$$Nu_{av.norm} = \frac{Nu_{av} - Nu_{av.min}}{Nu_{av.max} - Nu_{av.min}} \tag{28}$$

9. Results and Discussions

In combination, the numerical and graphical results show that the conflict between inertial, buoyancy, rheological, and nanoparticle-related phenomena control the heat-transfer behavior of the current non-Newtonian hybrid nanofluids system. Increasing (Re) leads to stronger circulation and forced convection, both of which enhance heat transfer. Increasing (Ri) improves thermal mixing by strengthening buoyancy-induced circulation. Within the studied range, increasing the volume percentage of nanoparticles alters the effective thermal characteristics and generally enhances thermal transfer. Conversely, raising the power-law index n reduces convective heat transfer by weakening circulation due to the increased apparent viscosity. The tendencies observed in the (Nu_{av}) data are clarified physically by the streamline and isotherm distributions. In particular, more distorted isotherms, thinner thermal boundary layers, and more heat penetration into the fluid domain are typically seen in cases linked to stronger circulation. On the other hand, bigger thermal boundary layers and smoother thermal contours result from weaker circulation. The RSM results also show that instead of functioning as totally independent parameters, (Re), (Ri), and (ϕ) interact nonlinearly. Although the very short dataset and the existence of multiple larger prediction errors necessitate careful interpretation, the ANN results show that it is feasible to use data-driven models to approximate the CFD-derived heat-transfer response.

10. Conclusion

The present study focuses on the mathematical examination of mixed convection transfer of energy involving two heated fins mounted on a heated vertical wall within a rectangular enclosure, using a non-Newtonian power-law hybrid nanofluid. The effects of several key non-dimensional parameters, namely the Reynolds number (Re), power-law index (n), Richardson number (Ri), and nanoparticle volume fraction (ϕ), are systematically examined to understand their influence on flow and heat transfer characteristics. Both numerical and graphical analyses are conducted to interpret the physical behavior of the system under different operating conditions. To ensure accuracy and stability in solving the governing equations, the numerical simulations are carried out using the finite element approach based on the Galerkin weighted residual formulation. To give a thorough understanding of the combined effects of forced and natural convection in the presence of non-Newtonian hybrid nanofluids, a variety of parameter values are taken into consideration. The results of this study provide important information on how the governing parameters affect the flow and temperature behavior inside the enclosure. These findings demonstrate significant patterns that can be applied to the design and optimization of thermal systems incorporating hybrid nanofluids, in addition to validating the suggested numerical model. Below is a synopsis of the main findings.

Author Contributions

Md. Noor-A-Alam Siddiki developed the approach, carried out the numerical simulations, analyzed and interpreted the findings, and created the initial text. Md. Shahinur Islam participated in the approach, verified the numerical results, helped analyze and interpret the data, and critically examined and rewrote the article. F. Habiba participated in the critical revision, editing, data interpretation, and literature review. The manuscript was written through the contribution of all authors. All authors discussed the results, reviewed, and approved the final version of the manuscript.

Acknowledgments

The authors would like to express their gratitude to their institutions for their support and encouragement throughout this research.

Conflict of Interest

The authors declared no potential conflicts of interest concerning the research, authorship, and publication of this article.

Funding

The authors received no financial support for the research, authorship, and publication of this article.

Data Availability Statements

The datasets generated and/or analyzed during the current study are available from the corresponding author on reasonable request.

Nomenclature

C_p	Specific heat capacity [J/kg K]	α	Thermal diffusivity [m²/s]
G	Gravitational acceleration [m/s²]	β	Thermal expansion coefficient [1/K]
Gr	Grashof number	ΔT	Temperature difference [K]
H	Characteristic height [m]	δ	Convergence tolerance
k	Thermal conductivity [W/m K]	μ	Dynamic viscosity [Pa·s]
n	Power-law index	ν	Kinematic viscosity [m²/s]
Nu_{av}	Average Nusselt number	ρ	Density [kg/m³]
P	Pressure [Pa]	θ	Dimensionless temperature
Pr	Prandtl number	ϕ	Nanoparticle volume fraction
Re	Reynolds number	Ri	Richardson number
T	Temperature [K]	t	Dimensionless time
u	Dimensionless velocity in x-direction	U_{in}	Inlet velocity [m/s]
v	Dimensionless velocity in y-direction	W	Characteristic width [m]
X	Dimensionless xx-coordinate	y	Dimensionless y-coordinate
C	Cold wall	f	Base fluid
H	Heated/Hot wall	*hnf*	Hybrid nanofluids
In	Inlet	*nf*	Nanofluid
Out	Outlet		

References

[1] Alarabi, T. H., Mahdy, A., Alotaibi, M. A., Aly, A. M., Abdelsalam, S., Artificial intelligence-powered magnetorheological dynamics of a dusty nanofluid: employing artificial neural network and hybrid fourth-order numerical methods, *Nanoscience and Technology: An International Journal*, 2025.
[2] Aly, A. M., Alotaibi, M., Asai, M., Abdelsalam, S. I., Meshfree simulation and artificial-intelligence enabled prediction of heat and mass transfer in a wavy annular cavity filled with a nanofluid and a heterogeneous porous medium containing hexagonal inserts, *Engineering Applications of Artificial Intelligence*, 181, 2026, 115229.
[3] Alsedais, N., Mansour, M. A., Aly, A. M., Abdelsalam, S. I., Artificial neural network validation of MHD natural bioconvection in a square enclosure: entropic analysis and optimization, *Acta Mechanica Sinica*, 41(9), 2025, 724507.
[4] Elsedais, N., Mansour, M. A., Aly, A. M., Abdelsalam, S., Artificial intelligence-driven FVM-ANN model for entropy analysis of MHD natural bioconvection in nanofluid-filled porous cavities, *Frontiers in Heat and Mass Transfer*, 22, 2024, 1277-1307.
[5] Sharma, R. P., Mishra, S. R., Metal and metallic oxide nanofluid over a shrinking surface with thermal radiation and heat generation/absorption, *Journal of Applied and Computational Mechanics*, 8(2), 2022, 557–565.
[6] Srivastava, R., Sharma, R. P., Central composite design-based parametric study of magnetically dissipative Darcy–Forchheimer hybrid nanofluid flow over an expanding sheet, *Journal of Applied and Computational Mechanics*, 12(3), 2026, 1035–1046.
[7] Srivastava, R., Sharma, R. P., Response surface method-based optimization of thermal transfer rate in hybrid nanofluid flow over a porous stretching sheet with multiple slip condition, *Journal of Applied and Computational Mechanics*, 12(2), 2026, 491–501.
[8] Sharma, A., Sharma, R. P., A critical review of non-Newtonian Sisko fluid and its role in industrial engineering, *Archives of Computational Methods in Engineering*, 2026, 1–30.
[9] Husainy, A. S. N., Kale, S. K., Sawant, S. M., Sur, A., Patil, S. D., Heat transfer phenomenon of nano-enhanced phase change material (NEPCM) incorporated in refrigeration test rig, *ES Energy & Environment*, 23, 2024, 1099.
[10] Sourtiji, E., Gorji-Bandpy, M., Ganji, D. D., Hosseinizadeh, S. F., Numerical analysis of mixed convection heat transfer of Al2O3-water nanofluid in a ventilated cavity considering different positions of the outlet port, *Powder Technology*, 262, 2014, 71–81.
[11] Abu-Nada, E., Chamkha, A. J., Mixed convection flow in a lid-driven inclined square enclosure filled with a nanofluid, *European Journal of Mechanics B/Fluids*, 29(6), 2010, 472–482.
[12] Nield, D. A., Simmons, C. T., A brief introduction to convection in porous media, *Transport in Porous Media*, 130(1), 2019, 237–250.
[13] Arani, A. A., Sebdani, S. M., Mahmoodi, M., Ardeshiri, A., Aliakbari, M., Numerical study of mixed convection flow in a lid-driven cavity with sinusoidal heating on sidewalls using nanofluid, *Superlattices and Microstructures*, 51(6), 2012, 893–911.
[14] Wang, X. Q., Mujumdar, A. S., Heat transfer characteristics of nanofluids: a review, *International Journal of Thermal Sciences*, 46(1), 2007, 1–19.
[15] Rasheed, T., Hussain, T., Anwar, M. T., Ali, J., Rizwan, K., Bilal, M., Alshammari, F. H., Alwadai, N., Almuslem, A. S., Hybrid nanofluids as renewable and sustainable colloidal suspensions for potential photovoltaic/thermal and solar energy applications, *Frontiers in Chemistry*, 9, 2021, 737033.
[16] Bhattad, A., Atgur, V., Rao, B. N., Banapurmath, N. R., Khan, T. M. Y., Vadlamudi, C., Krishnappa, S., Sajjan, A. M., Shankara, R. P., Ayachit, N. H., Review on mono and hybrid nanofluids: preparation, properties, investigation, and applications in IC engines and heat transfer, *Energies*, 16(7), 2023, 3189.
[17] Esfe, M. H., Saedodin, S., Yan, W. M., Afrand, M., Sina, N., Study on thermal conductivity of water-based nanofluids with hybrid suspensions of CNTs/Al2O3 nanoparticles, *Journal of Thermal Analysis and Calorimetry*, 124(1), 2016, 455–460.

[18] Chabani, I., Mebarek-Oudina, F., Ismail, A. A. I., MHD flow of a hybrid nanofluid in a triangular enclosure with zigzags and an elliptic obstacle, *Micromachines*, 13(2), 2022, 224.
[19] Ganeshkumar, P., Vinothkumar, S., Sundaram, P., Sathishkumar, A., Kim, S. C., Ramkumar, V., Pandiaraj, S., Alodhayb, A. N., Alzahrani, K. E., Performance evaluation of shot-blasted heat exchangers with MWCNT and activated carbon nanofluids: assessing entropy, exergy, sustainability index, Grashof, Rayleigh, and Richardson numbers for solar thermal applications, *Journal of Thermal Analysis and Calorimetry*, 149(22), 2024, 13285–13308.
[20] Rahman, M. A., Hasnain, S. M., Pandey, S., Tapalova, A., Akylbekov, N., Zairov, R., Review on nanofluids: preparation, properties, stability, and thermal performance augmentation in heat transfer applications, *ACS Omega*, 9(30), 2024, 32328–32349.
[21] Haque, M. R., Wasif, M., Mishal, K. A., Haque, M. M., Numerical investigation of MHD mixed convection phenomenon in a lid-driven hexagonal enclosure with wavy wall and SWCNT-MWCNT nanofluids, *Arabian Journal for Science and Engineering*, 48(3), 2023, 3863–3880.
[22] Das, P. K., Santra, A. K., Ganguly, R., Dash, S. K., Muthusamy, S., Sha, M. S., Sadasivuni, K. K., An extensive review of preparation, stabilization, and application of single and hybrid nanofluids, *Journal of Thermal Analysis and Calorimetry*, 149(17), 2024, 9523–9557.
[23] Hossain, A., Molla, M. M., Kamrujjaman, M., Mohebujjaman, M., Saha, S. C., MHD mixed convection of non-Newtonian Bingham nanofluid in a wavy enclosure with temperature-dependent thermophysical properties: a sensitivity analysis by response surface methodology, *Energies*, 16(11), 2023, 4408.
[24] Arafa, A. A. M., Rashed, Z. Z., Ahmed, S. E., Radiative flow of non-Newtonian nanofluids within inclined porous enclosures with time fractional derivative, *Scientific Reports*, 11(1), 2021, 5338.
[25] Srinivas, A. T., Bharti, R. P., Chhabra, R. P., Mixed convection heat transfer from a cylinder in power-law fluids: effect of aiding buoyancy, *Industrial & Engineering Chemistry Research*, 48(21), 2009, 9735–9754.
[26] Mahmood, F. T., Chowdhury, T. S., Hasan, M. N., Fluid-structure interaction induced mixed convection characteristics in a lid-driven square cavity with non-Newtonian power law fluids, *International Journal of Thermofluids*, 22, 2024, 100687.
[27] Korukçu, M. Ö., Heat transfer and entropy generation for mixed convection of Al_2O_3-water nanofluid in a lid-driven square cavity with a concentric square blockage, *Processes*, 12(6), 2024, 1079.
[28] Santhosh, N., Sivaraj, R., Prasad, V. R., Bég, O. A., Leung, H. H., Kamalov, F., Kuharat, S., Computational study of MHD mixed convective flow of Cu/Al_2O_3-water nanofluid in a porous rectangular cavity with slits, viscous heating, Joule dissipation and heat source/sink effects, *Waves in Random and Complex Media*, 36, 2026, 2241-2274.
[29] Dorel, V., Le Gal, P., Le Bars, M., Experimental study of the penetrative convection in gases, *Physical Review Fluids*, 8(10), 2023, 103501.
[30] Prabakaran, R., Eswaramoorthi, S., Loganathan, K., Sarris, I. E., Investigation on thermally radiative mixed convective flow of carbon nanotubes/Al_2O_3 nanofluid in water past a stretching plate with Joule heating and viscous dissipation, *Micromachines*, 13(9), 2022, 1424.
[31] Sarker, S. P. K., Alam, M. M., Numerical study of heat transfer in a nanofluid-filled trapezoidal enclosure with star-shaped heat sources under magnetic field, *Open Journal of Fluid Dynamics*, 15(3), 2025, 136–157.
[32] Al-Farhany, K., Al-Muhja, B., Loganathan, K., Periyasamy, U., Ali, F., Sarris, I. E., Analysis of convection phenomenon in enclosure utilizing nanofluids with baffle effects, *Energies*, 15(18), 2022, 6615.
[33] Mehmood, K., Hussain, S., Sagheer, M., Mixed convection in alumina-water nanofluid filled lid-driven square cavity with an isothermally heated square blockage inside with magnetic field effect: Introduction, *International Journal of Heat and Mass Transfer*, 109, 2017, 397–409.
[34] Shahi, M., Mahmoudi, A. H., Talebi, F., Numerical study of mixed convective cooling in a square cavity ventilated and partially heated from the below utilizing nanofluid, *International Communications in Heat and Mass Transfer*, 37(2), 2010, 201–213.
[35] Çakmak, N. K., Durmazuçar, H. H., Yapıcı, K., A numerical study of mixed convection heat transfer in a lid-driven cavity using Al2O3-water nanofluid, *International Journal of Chemistry and Technology*, 4(1), 2020, 22–37.
[36] Chowdhury, M. M. U., Islam, M. M., Hossain, M. Z., Molla, M. M., Magnetohydrodynamics mixed convection and sensitivity analysis of non-Newtonian power-law fluid in a ventilated cavity with a rotating heated cylinder, *Journal of Taibah University for Science*, 18(1), 2024, 2427386.
[37] Islam, A. W., Sharif, M. A. R., Carlson, E. S., Mixed convection in a lid-driven square cavity with an isothermally heated square blockage inside, *International Journal of Heat and Mass Transfer*, 55(19–20), 2012, 5244–5255.
[38] Karbasifar, B., Akbari, M., Toghraie, D., Mixed convection of water aluminum oxide nanofluid in an inclined lid-driven cavity containing a hot elliptical centric cylinder, *International Journal of Heat and Mass Transfer*, 116, 2018, 1237–1249.
[39] El-Shorbagy, M. A., Eslami, F., Ibrahim, M., Barnoon, P., Xia, W. F., Toghraie, D., Numerical investigation of mixed convection of nanofluid flow in a trapezoidal channel with different aspect ratios in the presence of porous medium, *Case Studies in Thermal Engineering*, 25, 2021, 100977.
[40] Abdulsahib, A. D., Alkhafaji, D., Albayati, I. M., A comprehensive review of the influence of various parameters on convection in different enclosures and heat sinks, *Journal of Thermal Analysis and Calorimetry*, 150(5), 2025, 3091–3119.
[41] Apmann, K., Fulmer, R., Soto, A., Vafaei, S., Thermal conductivity and viscosity: Review and optimization of effects of nanoparticles, *Materials*, 14(5), 2021, 1291.
[42] Shoeibi, S., Kargarsharifabad, H., Sharifpur, M., Meyer, J. P., Hybrid nanofluid natural convection in the square enclosure with periodic magnetic field: experimental investigation and economic evaluation, *Journal of Thermal Analysis and Calorimetry*, 148(6), 2023, 2527–2545.
[43] Kalsi, S., Kumar, S., Kumar, A., Alam, T., Sharma, A., Yadav, A. S., A review on hybrid nanofluids for heat transfer: advancements, synthesis, challenges and applications, *Discover Applied Sciences*, 7(7), 2025, 698.
[44] Rehman, N., Mahmood, R., Majeed, A. H., Khan, I., Mohamed, A., Multigrid simulations of non-Newtonian fluid flow and heat transfer in a ventilated square cavity with mixed convection and baffles, *Scientific Reports*, 14(1), 2024, 6694.
[45] Hossain, M. A., Sajib, M. A. H., Sagib, M., Islam, M. R., Barai, G., Podder, C., Saha, B. K., Enhanced thermal efficiency on mixed convection flow of TiO_2-water nanofluid inside a double lid-driven zigzag cavity with and without heated obstacles insertion, *International Journal of Thermofluids*, 25, 2025, 101040.
[46] Siddiki, M. N. A. A., Islam, S., Ahmmed, M. U., Hasan, M. F., Molla, M. M., A study of forced convection in non-Newtonian hybrid nanofluids embedded in a heated cylinder within a hexagonal enclosure by finite element method, *Mathematics*, 13(3), 2025, 445.
[47] Alsabery, A. I., Tayebi, T., Kadhim, H. T., Ghalambaz, M., Hashim, I., Chamkha, A. J., Impact of two-phase hybrid nanofluid approach on mixed convection inside wavy lid-driven cavity having localized solid block, *Journal of Advanced Research*, 30, 2021, 63–74.
[48] Eshaghi, S., Izadpanah, F., Dogonchi, A. S., Chamkha, A. J., Ben Hamida, M. B., Alhumade, H., The optimum double diffusive natural convection heat transfer in H-shaped cavity with a baffle inside and a corrugated wall, *Case Studies in Thermal Engineering*, 28, 2021, 101541.
[49] Alsabery, A. I., Hashim, I., Hajjar, A., Ghalambaz, M., Nadeem, S., Saffari Pour, M., Entropy generation and natural convection flow of hybrid nanofluids in a partially divided wavy cavity including solid blocks, *Energies*, 13(11), 2020, 2942.
[50] Ma, Y., Mohebbi, R., Rashidi, M. M., Yang, Z., MHD convective heat transfer of Ag-MgO/water hybrid nanofluid in a channel with active heaters and coolers, *International Journal of Heat and Mass Transfer*, 137, 2019, 714–726.
[51] Tiwari, R. K., Das, M. K., Heat transfer augmentation in a two-sided lid-driven differentially heated square cavity utilizing nanofluids, *International Journal of Heat and Mass Transfer*, 50(9–10), 2007, 2002–2018.
[52] Oztop, H. F., Abu-Nada, E., Numerical study of natural convection in partially heated rectangular enclosures filled with nanofluids, *International Journal of Heat and Fluid Flow*, 29(5), 2008, 1326–1336.
[53] Basak, T., Roy, S., Thirumalesha, Ch., Finite element analysis of natural convection in a triangular enclosure: effects of various thermal boundary conditions, *Chemical Engineering Science*, 62(9), 2007, 2623–2640.
[54] Siddiki, M. N. A. A., Islam, S., Ahmmed, M. U., Molla, M. M., Numerical simulation of a non-Newtonian nanofluid on mixed convection in a rectangular enclosure with two rotating cylinders, *International Journal of Ambient Energy*, 45(1), 2024, 2332525.
[55] Moukalled, F., Darwish, M., A new family of streamline-based very-high-resolution schemes, *Numerical Heat Transfer*, 32(3), 1997, 299–320.
[56] Islam, S., Islam, M. M., Rana, B. M. J., Islam, M. S., Reza-E-Rabbi, S. K., Hossain, M. S., Rahman, M. M., Numerical investigation with sensitivity study of MHD mixed convective hexagonal heat exchanger using TiO2-H2O nanofluid, *Results in Engineering*, 18, 2023, 101136.
[57] Nasir, S., Berrouk, A. S., Comparative study of computational frameworks for magnetite and carbon nanotube-based nanofluids in enclosure, *Journal of Thermal Analysis and Calorimetry*, 149(5), 2024, 2403–2423.
[58] Islam, T., Gama, S., Afonso, M. M., Artificial neural network and response surface methodology-driven optimization of Cu–Al2O3/water hybrid nanofluid flow in a wavy enclosure with inclined periodic magnetohydrodynamic effects, *Mathematics*, 13(1), 2024, 78.

[59] Montgomery, D. C., *Design and Analysis of Experiments*, John Wiley & Sons, 2017.
[60] Kshirsagar, D. P., Venkatesh, M. A., A review on hybrid nanofluids for engineering applications, *Materials Today: Proceedings*, 44, 2021, 744–755.

ORCID iD

Md. Noor-A-Alam Siddiki https://orcid.org/0009-0007-2411-5995
Md. Shahinur Islam https://orcid.org/0009-0003-1383-3263
Farjana Habiba https://orcid.org/0009-0009-7690-7366

© 2026 Shahid Chamran University of Ahvaz, Ahvaz, Iran. This article is an open access article distributed under the terms and conditions of the Creative Commons Attribution-NonCommercial 4.0 International (CC BY-NC 4.0 license) (http://creativecommons.org/licenses/by-nc/4.0/).

How to cite this article: Noor-A-Alam Siddiki Md., Shahinur Islam Md., Habiba F. Comparative Analysis of Artificial Neural Networks and Response Surface Methods for Mixed Convective Heat Transfer in a Rectangular Channel with Heated Diamond-Shaped Obstacles, *J. Appl. Comput. Mech.*, xx(x), 2026, 1–16. https://doi.org/10.22055/jacm.2026.49656.6137

Publisher's Note Shahid Chamran University of Ahvaz remains neutral with regard to jurisdictional claims in published maps and institutional affiliations.